Discrete modes and continuous spectra in supersonic boundary layers

By P. BALAKUMAR and M. R. MALIK

High Technology Corporation, P.O. Box 7262, Hampton, VA 23666, USA

The disturbance field induced due to a harmonic point source consists of discrete eigenmodes and a continuous spectrum; these are studied by using generalized Fourier transform techniques. For a supersonic boundary layer, there exist seven branches of the continuous spectrum in the complex wavenumber space, four of which (two acoustic waves, one vorticity wave and one entropy wave) contribute to the flow field downstream of the source. The discrete eigenmodes spring off from these branches at some critical Reynolds numbers. The results for Mach 2 and 4.5 boundary layers show that the receptivity coefficients for the stable discrete modes are much larger than that for the unstable mode. Therefore, the flow very near the source is dominated by the continuous spectrum and the stable discrete modes. However, the unstable mode takes over sufficiently far away from the source. It is shown that it is only necessary to consider the first few discrete modes to construct the solution. Calculations also show that, in a supersonic boundary layer, upstream influence from a localized disturbance is minimal.

1. Introduction

When a localized disturbance is introduced into a boundary layer, the disturbance field can be divided into two regions: one near the source and the other further downstream of the source. The flow field in the near-field region consists of all the discrete eigensolutions and the continuous spectrum which appears because the domain is unbounded and the governing differential equations admit solutions which are bounded at infinity. Since the continuous spectrum decays algebraically away from the source, contributions from the continuous spectrum can be neglected in the far field. Among the discrete eigensolutions, only one or a few, at most, may be unstable and grow exponentially downstream of the source and all the others will decay exponentially. Therefore, the disturbances in the far field consist of only the exponentially growing discrete modes.

In this paper we investigate the disturbance field near the source, and in a subsequent paper we investigate the disturbance field in the downstream of the source. The disturbances are introduced from a localized harmonic point source, figure 1. Thus, a wide band of spanwise wavenumbers is excited at the frequency of oscillation of the source. This problem can be considered as a model for studying the boundary-layer instability waves which are generated at isolated roughness sites or surface imperfections due to interaction with free-stream disturbances of a given frequency.

$$v_0 = \sin \omega t \delta(z) \delta(x - x_0)$$

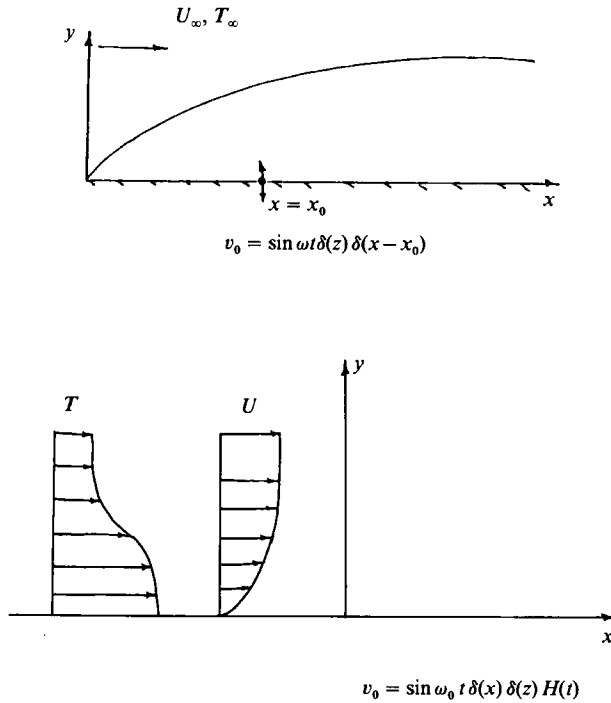$$v_0 = \sin \omega_0 t \delta(x) \delta(z) H(t)$$

FIGURE 1. Schematic diagram.

Our objective is to consider compressible, flat-plate boundary-layer flows. Most previous investigations have considered incompressible flows. For example, Mack (1976) studied the stability of Blasius flow using the Orr–Sommerfeld equation and found that there exist only seven discrete eigenvalues in the complex frequency plane and only one, if it exists, is unstable. Although the number of eigenvalues varies with Reynolds number and wavenumber or frequency, for an infinite domain there is only a finite, and small, number of discrete modes, which cannot be used to represent an arbitrary disturbance. The finiteness of the discrete mode spectrum for incompressible Blasius flow was proved by Miklavcic & Williams (1982) and Miklavcic (1983). For a bounded domain, however, the Orr–Sommerfeld equation has a complete set of eigenfunctions and eigenvalues (see DiPrima & Habetler 1969). Hence, any smooth function can be expanded in terms of this complete eigenset. Recently, Henningson & Schmid (1991) used this approach to study the evolution of disturbances in plane channel flow.

Grosch & Salwen (1978) showed that the Orr–Sommerfeld equation in an unbounded domain has a continuous spectrum. As pointed out above, the continuous spectrum appears because the domain is unbounded and the governing equations admit solutions which are bounded at infinity. We note that the continuous spectrum in the Rayleigh equation, which has none or a small number of discrete modes depending upon the existence of inflection points in the mean flow profile, can also appear owing to the singularity which exists in the Rayleigh equation. Salwen & Grosch (1981) showed that the set consisting of the discrete eigenmodes and continuum eigenfunctions is complete in the temporal Orr–Sommerfeld case. The solution of the initial-value problem of the linearized Navier–Stokes equations can be expanded as the sum of the discrete modes and some integral around the continuous

spectrum. The coefficients of these expansions are obtained from the initial disturbance using orthogonality conditions. Salwen & Grosch showed that in spatial theory the continuous spectrum consists of four branches in the complex wavenumber plane, and they derived the solution of the disturbance equation as a sum of discrete modes and continuous spectra. However, they considered only a semi-infinite streamwise domain in $x \in [0, \infty]$ and imposed the boundary condition at $x = 0$ for all times. They could not establish that in the spatial case the discrete modes and continuous spectrum form a complete set.

Gustavsson (1979) solved the linearized Navier–Stokes equations as an initial-value problem in the temporal case using Fourier and Laplace transform techniques. He showed that the branch cut in the Laplace inversion plane introduced the continuous spectrum, and derived the solution using the contour integral method. Salwen & Grosch (1981) showed that their formal expansion procedure and this residue integral method led to the same result. Murdock & Stewartson (1977), using the heat conduction equation as a model equation, investigated the spectra of the Orr–Sommerfeld equation. They showed that the contribution from the continuous spectrum can be interpreted as the sum of discrete modes. Each discrete mode is represented by some integral over the continuous spectrum. They also verified that the number of discrete eigenvalues is finite in both the temporal and spatial cases and this number depends on the Reynolds number and wavenumber or frequency. Another interesting observation is that when these individual discrete modes are followed by decreasing the Reynolds number, the discrete modes are absorbed into the continuous spectrum at a 'critical' Reynolds number. This implies that when the Reynolds number is increased new discrete modes spring off from the continuous spectrum. Hence, the number of discrete modes will increase with Reynolds number. The above observation also suggests that the continuous spectrum may have a role to play in boundary-layer receptivity to free-stream disturbances.

Recently Ashpis & Reshotko (1990) considered the vibrating ribbon problem as an initial-value problem and obtained a long-time solution using the Briggs (1964) method and the contour integration technique. They derived the expressions for the four branches of the continuous spectrum and found the solution in terms of discrete modes and some integrals over the continuous spectrum. However, no quantitative results were given

For compressible boundary layers, Tumin & Fedorov (1983) investigated the continuous spectrum and found that there exist seven branch cuts in the complex wavenumber space. They computed these branch cuts for two-dimensional disturbances at two different Mach numbers. In this paper, we also consider compressible boundary layers and investigate the flow field near the source, which is represented by all the discrete modes and the continuous spectrum. In §2 we formulate the problem in a way similar to Gaster (1965) and Ashpis & Reshotko (1990), where the solution is sought using Fourier and Laplace transform techniques. Results for Mach 2 and 4.5 boundary layers are presented in §3. The results include: (i) the branch cuts and branch points of the continuous spectrum, (ii) the discrete modes, (iii) the locus of these modes with Reynolds number and (iv) the contribution to the solution from the discrete modes and continuous spectrum. A discussion and conclusions are presented in §4.

2. Formulation of the problem

We consider two-dimensional, compressible boundary-layer flow over an insulated flat plate. A harmonic point source of disturbances is embedded in the wall at a streamwise location $x = x_0$ (see figure 1). The distance normal to the plate is measured by coordinate y while z represents the spanwise coordinate. The x, y, z components of velocity are represented by U, V, W, respectively, and pressure, density and temperature of the gas by P, ρ, T. The corresponding disturbance quantities are denoted by $(u, v, w, p, \tau, \theta)$. We are interested in the response of the boundary layer to a three-dimensional harmonic excitation of a point source starting impulsively at time $t = 0$. Since we are interested in the flow field near the source, it is reasonable to assume that the basic flow is parallel to the x-axis, i.e. the mean flow is given as $(U(y), 0, 0, P(y), \rho(y), T(y))$. The flow field further away from the source is studied in a follow-up paper using a non-parallel approach. The linearized, non-dimensionalized Navier–Stokes, energy, continuity and state equations are

$$\rho\left(\frac{\partial u}{\partial t}+U\frac{\partial u}{\partial x}+v\frac{\mathrm{d}U}{\mathrm{d}y}\right)=-\frac{\partial p}{\partial x}+\frac{1}{\mathrm{Re}}\left[2\mu\frac{\partial^2 u}{\partial x^2}+\mu\left(\frac{\partial^2 u}{\partial y^2}+\frac{\partial^2 u}{\partial z^2}+\frac{\partial^2 v}{\partial x\,\partial y}+\frac{\partial^2 w}{\partial x\,\partial z}\right)\right.$$

$$\left.-\tfrac{2}{3}\mu\left(\frac{\partial^2 u}{\partial x^2}+\frac{\partial^2 v}{\partial x\,\partial y}+\frac{\partial^2 w}{\partial x\,\partial z}\right)+\frac{\mathrm{d}\mu}{\mathrm{d}T}\frac{\mathrm{d}T}{\mathrm{d}y}\left(\frac{\partial u}{\partial y}+\frac{\partial v}{\partial x}\right)+\frac{\mathrm{d}\mu}{\mathrm{d}T}\left(\frac{\mathrm{d}^2 U}{\mathrm{d}y^2}\theta+\frac{\mathrm{d}U}{\mathrm{d}y}\frac{\partial\theta}{\partial y}\right)+\frac{\mathrm{d}^2\mu}{\mathrm{d}T^2}\frac{\mathrm{d}T}{\mathrm{d}y}\frac{\mathrm{d}U}{\mathrm{d}y}\theta\right], \tag{2.1}$$

$$\rho\left(\frac{\partial v}{\partial t}+U\frac{\partial v}{\partial x}\right)=-\frac{\partial p}{\partial y}+\frac{1}{\mathrm{Re}}\left[2\mu\frac{\partial^2 v}{\partial y^2}+\mu\left(\frac{\partial^2 v}{\partial x^2}+\frac{\partial^2 v}{\partial z^2}+\frac{\partial^2 u}{\partial x\,\partial y}+\frac{\partial^2 w}{\partial y\,\partial z}\right)-\tfrac{2}{3}\mu\left(\frac{\partial^2 u}{\partial x\,\partial y}+\frac{\partial^2 v}{\partial y^2}+\frac{\partial^2 w}{\partial y\,\partial z}\right)\right.$$

$$\left.+\frac{\mathrm{d}\mu}{\mathrm{d}T}\left(2\frac{\mathrm{d}T}{\mathrm{d}y}\frac{\partial v}{\partial y}+\frac{\mathrm{d}U}{\mathrm{d}y}\frac{\partial\theta}{\partial x}\right)-\frac{2}{3}\frac{\mathrm{d}\mu}{\mathrm{d}T}\frac{\mathrm{d}T}{\mathrm{d}y}\left(\frac{\partial u}{\partial x}+\frac{\partial v}{\partial y}+\frac{\partial w}{\partial z}\right)\right], \tag{2.2}$$

$$\rho\left(\frac{\partial w}{\partial t}+U\frac{\partial w}{\partial x}\right)=-\frac{\partial p}{\partial z}+\frac{1}{\mathrm{Re}}\left[2\mu\frac{\partial^2 w}{\partial z^2}+\mu\left(\frac{\partial^2 w}{\partial y^2}+\frac{\partial^2 w}{\partial x^2}+\frac{\partial^2 v}{\partial y\,\partial z}+\frac{\partial^2 u}{\partial x\,\partial z}\right)\right.$$

$$\left.-\tfrac{2}{3}\mu\left(\frac{\partial^2 w}{\partial z^2}+\frac{\partial^2 v}{\partial y\,\partial z}+\frac{\partial^2 u}{\partial x\,\partial z}\right)+\frac{\mathrm{d}\mu}{\mathrm{d}T}\frac{\mathrm{d}T}{\mathrm{d}y}\left(\frac{\partial w}{\partial y}+\frac{\partial v}{\partial z}\right)\right], \tag{2.3}$$

$$\rho\left(\frac{\partial\theta}{\partial t}+U\frac{\partial\theta}{\partial x}+v\frac{\mathrm{d}T}{\mathrm{d}y}\right)=-(\gamma-1)\left(\frac{\partial u}{\partial x}+\frac{\partial v}{\partial y}+\frac{\partial w}{\partial z}\right)+\frac{\gamma}{\sigma\,\mathrm{Re}}\left[\mu\left(\frac{\partial^2\theta}{\partial x^2}+\frac{\partial^2\theta}{\partial y^2}+\frac{\partial^2\theta}{\partial z^2}\right)\right.$$

$$\left.+\frac{\mathrm{d}\mu}{\mathrm{d}T}\frac{\mathrm{d}^2 T}{\mathrm{d}y^2}\theta+2\frac{\mathrm{d}\mu}{\mathrm{d}T}\frac{\mathrm{d}T}{\mathrm{d}y}\frac{\partial\theta}{\partial y}+\frac{\mathrm{d}^2\mu}{\mathrm{d}T^2}\left(\frac{\mathrm{d}T}{\mathrm{d}y}\right)^2\theta\right]+\frac{\gamma(\gamma-1)}{\mathrm{Re}}M^2\left[2\mu\frac{\mathrm{d}U}{\mathrm{d}y}\left(\frac{\partial u}{\partial y}+\frac{\partial v}{\partial x}\right)+\frac{\mathrm{d}\mu}{\mathrm{d}T}\left(\frac{\mathrm{d}U}{\mathrm{d}y}\right)^2\theta\right], \tag{2.4}$$

$$\frac{\partial\tau}{\partial t}+\rho\left(\frac{\partial u}{\partial x}+\frac{\partial v}{\partial y}+\frac{\partial w}{\partial z}\right)+v\frac{\mathrm{d}\rho}{\mathrm{d}y}+U\frac{\partial\tau}{\partial x}=0, \tag{2.5}$$

$$\gamma M^2 p = \rho\theta+\tau T. \tag{2.6}$$

Here the variables are non-dimensionalized as follows: velocity by U_∞, temperature by T_∞, density by ρ_∞, pressure by $\rho_\infty U_\infty^2$, length by $(\nu_\infty x_0/U_\infty)^{\frac{1}{2}}$, and time by $(\nu_\infty x_0)^{\frac{1}{2}}/U_\infty^{\frac{3}{2}}$, where U_∞, T_∞, ρ_∞, P_∞, ν_∞ are free-stream velocity, temperature, density, pressure and kinematic viscosity. Stokes' hypothesis of vanishing bulk viscosity has been used here.

The non-dimensional quantities appearing in the equations are defined as follows: M is the free-stream Mach number, $U_\infty/(\gamma\mathscr{R}T_\infty)^{\frac{1}{2}}$; σ the Prandtl number, assumed to have the constant value of 0.72; γ the specific heat ratio, taken as 1.4; Re the Reynolds number, $(U_\infty x_0/\nu_\infty)^{\frac{1}{2}}$; and $\mathscr{R}$ the gas constant.

The boundary conditions at the wall are $u = \theta = w = 0$ and

$$v(x, 0, z, t) = \sin \omega_0 t \delta(x - x_0)\, \delta(z)\, H(t), \tag{2.7}$$

where ω_0 is the frequency of oscillation of the point source, δ is Dirac's delta function and $H(t)$ is the unit step function, which indicates that the motion starts from rest at $t = 0$. We require that the disturbances decay far away from the plate.

The physical disturbance field may be related to the spectral space by using the generalized triple Fourier transform defined as

$$\tilde{\boldsymbol{\phi}}(k_x, y, k_z, \omega) = \int_{-\infty}^\infty \mathrm{d}t \int_{-\infty}^\infty \mathrm{d}x \int_{-\infty}^\infty \mathrm{d}z\, \boldsymbol{\phi}(x, y, z, t)\, \mathrm{e}^{-\mathrm{i}(k_x x + k_z z - \omega t)}, \tag{2.8}$$

where k_x, k_z are the complex wavenumbers in the (x, z)-directions, ω is the complex frequency, $\boldsymbol{\phi} = \{u, v, w, \theta, p\}^{\mathrm{T}}$, and $\tilde{\boldsymbol{\phi}} = \{\tilde{u}, \tilde{v}, \tilde{w}, \tilde{\theta}, \tilde{p}\}^{\mathrm{T}}$. Here, the tilde represents the transformed variable and superscript T represent the transpose of a matrix. Since $\boldsymbol{\phi}$ is a causal function in t, the Fourier transform in time is equivalent to the Laplace transform in time. Thus, (2.1)–(2.6) can be transformed using (2.8) into the following system of equations for $\tilde{\boldsymbol{\phi}}$:

$$\boldsymbol{A}\frac{\mathrm{d}^2\tilde{\boldsymbol{\phi}}}{\mathrm{d}y^2} + \boldsymbol{B}\frac{\mathrm{d}\tilde{\boldsymbol{\phi}}}{\mathrm{d}y} + \boldsymbol{C}\tilde{\boldsymbol{\phi}} = 0, \tag{2.9}$$

where $\boldsymbol{A}$, $\boldsymbol{B}$, $\boldsymbol{C}$ are $[5 \times 5]$ matrices whose coefficients are given in Malik (1990). Transforming the boundary conditions yields

$$\tilde{v}(k_x, 0, k_z, \omega) = -\frac{\omega_0}{\omega^2 - \omega_0^2}, \tag{2.10}$$

$$\tilde{u} = \tilde{w} = \tilde{\theta} = 0 \quad \text{at} \quad y = 0, \tag{2.11}$$

and
$$\tilde{\boldsymbol{\phi}} \to 0 \quad \text{as} \quad y \to \infty. \tag{2.12}$$

Equations (2.9)–(2.12) form a non-homogeneous system, where the non-homogeneity is due to the oscillation of the source at frequency ω_0. The solution of (2.9) can be written as

$$\tilde{\boldsymbol{\phi}}(k_x, y, k_z, \omega) = \sum_{i=1}^8 C_i \tilde{\boldsymbol{\phi}}_i \tag{2.13}$$

where $\tilde{\boldsymbol{\phi}}_i$ $(i = 1, 8)$ represent the eight fundamental solutions of (2.9). The C_i $(i = 1, 8)$ are integration constants which can be determined from the boundary conditions (2.10)–(2.12).

As $y \to \infty$, (2.9) is simplified to

$$\tilde{u}'' + \tfrac{1}{3}\mathrm{i}k_x\tilde{v}' + \tilde{u}\{-\mathrm{i}(k_x - \omega)Re - \tfrac{4}{3}k_x^2 - k_z^2\} - \tfrac{1}{3}k_x k_z\tilde{w} - \mathrm{i}k_x Re\,\tilde{p} = 0, \tag{2.14}$$

$$\tilde{w}'' + \tfrac{1}{3}\mathrm{i}k_z\tilde{v}' - \tfrac{1}{3}k_x k_z\tilde{u} + \tilde{w}\{-\mathrm{i}(k_x - \omega)Re - k_x^2 - \tfrac{4}{3}k_z^2\} - \mathrm{i}k_z Re\,\tilde{p} = 0, \tag{2.15}$$

$$\tilde{v}'' + \tfrac{1}{4}\mathrm{i}k_x\tilde{u}' + \tfrac{1}{4}\mathrm{i}k_z\tilde{w}' - \tfrac{4}{3}Re\,\tilde{p}' + \tilde{v}\{-\tfrac{3}{4}\mathrm{i}(k_x - \omega)Re - \tfrac{3}{4}k_x^2 - \tfrac{3}{4}k_z^2\} = 0, \tag{2.16}$$

$$\tilde{\theta}'' - \frac{(\gamma - 1)\sigma Re}{\gamma}\tilde{v}' - \frac{(\gamma - 1)\mathrm{i}k_x\sigma Re}{\gamma}\tilde{u} - \frac{(\gamma - 1)\mathrm{i}k_z}{\gamma}\sigma Re\,\tilde{w}$$
$$- \left\{\frac{\sigma Re\,\mathrm{i}(k_x - \omega)}{\gamma} + k_x^2 + k_z^2\right\}\tilde{\theta} = 0, \tag{2.17}$$

$$\tilde{v}' + \mathrm{i}k_x\tilde{u} + \mathrm{i}k_z\tilde{w} - \mathrm{i}(k_x - \omega)\tilde{\theta} + \mathrm{i}(k_x - \omega)\gamma M^2\tilde{p} = 0. \tag{2.18}$$

The solution of this system can be written as

$$\tilde{\phi} = \sum_{i=1}^{8} C_i \boldsymbol{q}_i \, \mathrm{e}^{r_i y},$$ (2.19)

where $\boldsymbol{q}_i$ ($i = 1, 8$) are column vectors and

$$r_1 = -\mu_1, \quad r_2 = -\mu_2, \quad r_3 = -\mu_3, \quad r_4 = -\mu_4, \quad r_5 = \mu_1, \quad r_6 = \mu_2, \quad r_7 = \mu_3, \quad r_8 = \mu_4;$$

$$\mu_1 = \lambda_1^{\frac{1}{2}}, \quad \mu_2 = \lambda_2^{\frac{1}{2}}, \quad \mu_3 = \lambda_3^{\frac{1}{2}}, \quad \mu_4 = \lambda_4^{\frac{1}{2}};$$

$$\lambda_1 = \lambda_2 = \mathrm{i}(k_x - \omega) \, Re + k_x^2 + k_z^2,$$ (2.20)

$$\lambda_3 = \tfrac{1}{2}[b_{22} + b_{23} + [(b_{22} + b_{33})^2 + 4(b_{23} b_{32} - b_{22} b_{33})]^{\frac{1}{2}}]$$ (2.21)

$$\lambda_4 = \tfrac{1}{2}[b_{22} + b_{23} - [(b_{22} + b_{33})^2 + 4(b_{23} b_{32} - b_{22} b_{33})]^{\frac{1}{2}}];$$ (2.22)

$$b_{22} = k_x^2 + k_z^2 - Re\,(k_x - \omega)^2 \frac{[\tfrac{3}{4}\gamma M^2 - (\gamma - 1)\,\sigma M^2]}{\tfrac{3}{4}Re + \mathrm{i}(k_x - \omega)\,\gamma M^2},$$ (2.23)

$$b_{23} = \frac{Re\,(k_x - \omega)^2 \{\tfrac{3}{4} - \sigma\}}{\tfrac{3}{4}Re + \mathrm{i}(k_x - \omega)\,\gamma M^2},$$ (2.24)

$$b_{32} = -\mathrm{i}(k_x - \omega)\,(\gamma - 1)\,\sigma M^2 \, Re,$$ (2.25)

$$b_{33} = \mathrm{i}(k_x - \omega)\,\sigma \, Re + k_x^2 + k_z^2.$$ (2.26)

Here the $\{\mu_i\}$ are single-valued functions obtained by taking the branch cut along the negative real $\{\lambda_i\}$ axes, choosing the branches of $\{\mu_i\}$ such that real parts of $\{\mu_i\}$ are greater than zero for all $\{\lambda_i\}$. Since $\tilde{\phi}_5$, $\tilde{\phi}_6$, $\tilde{\phi}_7$ and $\tilde{\phi}_8$ grow exponentially in y, the values of C_5, C_6, C_7 and C_8 have to be zero for the disturbance to decay in the far field.

The values C_1, C_2, C_3 and C_4 are obtained by applying the boundary conditions at the wall. They take the form

$$\{\boldsymbol{Q}\}[C_1, C_2, C_3, C_4]^{\mathrm{T}} = \left\{0, -\frac{\omega_0}{\omega^2 - \omega_0^2}, 0, 0\right\}^{\mathrm{T}},$$ (2.27)

where $\{\boldsymbol{Q}\}$ is a $[4 \times 4]$ matrix given by

$$\boldsymbol{Q} = \left\{ \begin{matrix} \tilde{\phi}_{11} & \tilde{\phi}_{21} & \tilde{\phi}_{31} & \tilde{\phi}_{41} \\ \tilde{\phi}_{12} & \tilde{\phi}_{22} & \tilde{\phi}_{32} & \tilde{\phi}_{42} \\ \tilde{\phi}_{13} & \tilde{\phi}_{23} & \tilde{\phi}_{33} & \tilde{\phi}_{43} \\ \tilde{\phi}_{14} & \tilde{\phi}_{24} & \tilde{\phi}_{34} & \tilde{\phi}_{44} \end{matrix} \right\},$$ (2.28)

where $\tilde{\phi}_{ij}$ represents the jth row of the solution $\tilde{\phi}_i$. Substituting for C_1, C_2, C_3 and C_4 in the expression for $\tilde{\phi}$, (2.13), we obtain

$$\tilde{\phi}(k_x, y, k_z, \omega) = -\frac{\omega_0}{\omega^2 - \omega_0^2} \frac{\tilde{\phi}_1 \varDelta_{12} + \tilde{\phi}_2 \varDelta_{22} + \tilde{\phi}_3 \varDelta_{32} + \tilde{\phi}_4 \varDelta_{42}}{\varDelta}$$ (2.29)

where $\varDelta$ is the determinant of the matrix $\boldsymbol{Q}$ and $\varDelta_{ij}$ is the cofactor of the matrix $\boldsymbol{Q}$. Before we proceed further we will examine (2.29). We observe that singularities of this equation appear in three ways. These singularities occur when $\omega^2 - \omega_0^2 = 0$, $\varDelta(k_x, k_z, \omega) = 0$ and also for singularities associated with $\tilde{\phi}_i$ ($i = 1, 4$). Here, $\varDelta = 0$ is the dispersion relation for the linear compressible stability equations.

Since the governing equation (2.9) is analytic in k_x, k_z and ω, singularities which can appear in $\tilde{\phi}_i$ are the branch-cut singularities associated with boundary conditions at the far field. The singularities $\omega^2 - \omega_0^2 = 0$ and $\varDelta = 0$ produce the normal mode
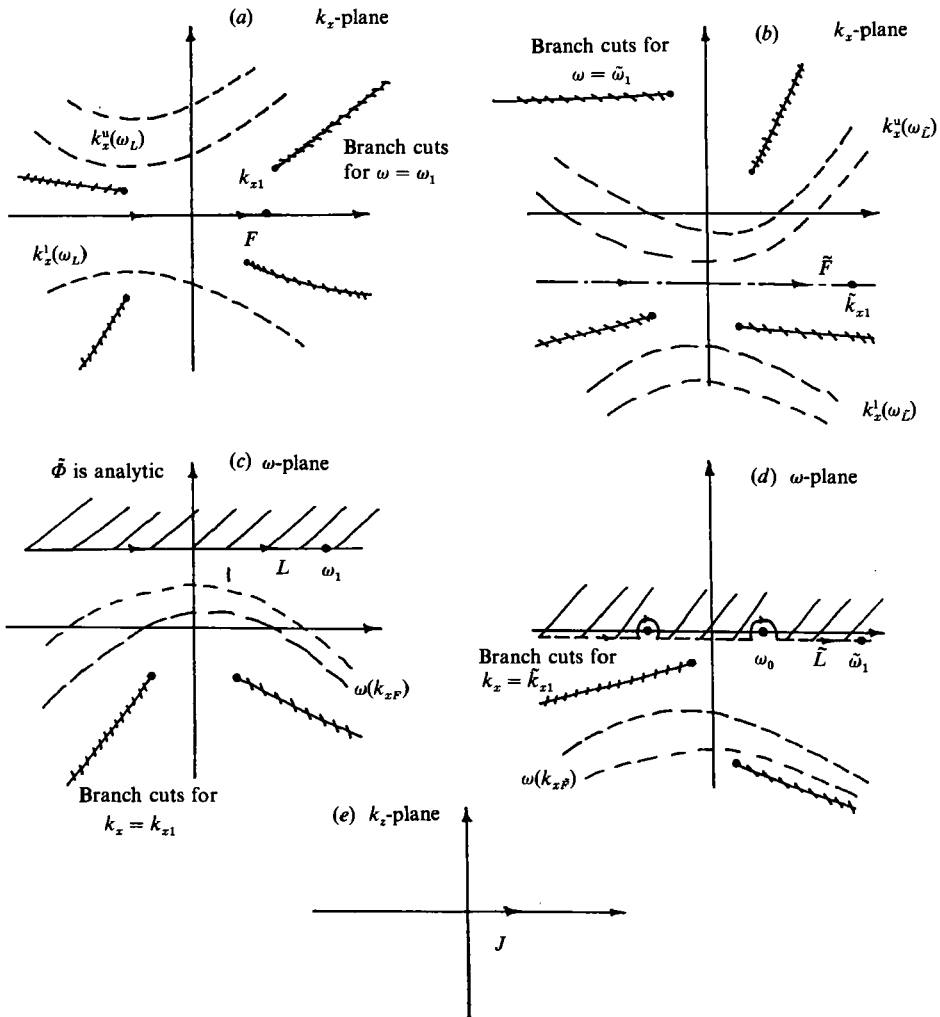
FIGURE 2. Integration paths in the complex k_x-, ω- and k_z-planes. F, L, J are the Fourier and Laplace inversion contours in the k_x-, ω- and k_z-planes before the deformation (a, c, e). $\tilde{F}$, $\tilde{L}$ are the Fourier and Laplace inversion contours in the k_x and ω planes after the deformation (b, d).

solutions, while the branch-cut singularities introduce the continuous spectrum solutions. We invert this expression for $\tilde{\phi}$, (2.29), from the Fourier space to physical space in order to obtain the disturbance quantities $\phi(x, y, z, t)$ and evaluate the solution for $t \to \infty$. To this end, we use the triple inverse Fourier transform defined as

$$\phi(x, y, z, t) = \frac{1}{(2\pi)^3} \int_J \mathrm{d}k_z \, \mathrm{e}^{\mathrm{i}k_z z} \int_L \mathrm{d}\omega \, \mathrm{e}^{-\mathrm{i}\omega t} \int_F \mathrm{e}^{\mathrm{i}k_x x} \, \tilde{\phi}(k_x, y, k_z, \omega) \, \mathrm{d}k_x, \qquad (2.30)$$

where J, L, F (see figure 2) are the inversion contours in the k_z-, ω- and k_x-planes, respectively. Substituting for $\tilde{\phi}$ from (2.29), we obtain

$$\phi(x, y, z, t) = \frac{1}{(2\pi)^3} \int_J \mathrm{d}k_z \, \mathrm{e}^{\mathrm{i}k_z z} \int_L \mathrm{d}\omega \left(\frac{-\omega_0}{\omega^2 - \omega_0^2} \right) \mathrm{e}^{-\mathrm{i}\omega t} \int_F \mathrm{e}^{\mathrm{i}k_x x} \, \tilde{\Phi}(k_x, y, k_z, \omega) \, \mathrm{d}k_x,$$

$$(2.31)$$

where
$$\tilde{\boldsymbol{\Phi}} = \frac{\tilde{\phi}_1 \varDelta_{12} + \tilde{\phi}_2 \varDelta_{22} + \tilde{\phi}_3 \varDelta_{32} + \tilde{\phi}_4 \varDelta_{42}}{\varDelta}. \tag{2.32}$$

From computational considerations, it is easier to solve for $\tilde{\boldsymbol{\Phi}}$ than for $\tilde{\phi}_1, \tilde{\phi}_2, \tilde{\phi}_3$ and $\tilde{\phi}_4$ separately. We see that $\tilde{\boldsymbol{\Phi}}$ satisfies the following equations:

$$\boldsymbol{A}\frac{\mathrm{d}^2\tilde{\boldsymbol{\Phi}}}{\mathrm{d}y^2} + \boldsymbol{B}\frac{\mathrm{d}\tilde{\boldsymbol{\Phi}}}{\mathrm{d}y} + \boldsymbol{C}\tilde{\boldsymbol{\Phi}} = 0, \tag{2.33}$$

$$\tilde{u} = \tilde{w} = \tilde{\theta} = 0 \quad \text{at} \quad y = 0 \tag{2.34}$$

$$\tilde{v}(y = 0) = 1. \tag{2.35}$$

Here $\tilde{\boldsymbol{\Phi}}$ is a 5-element vector whose elements are $\{\tilde{u}, \tilde{v}, \tilde{w}, \tilde{\theta}, \tilde{p}\}$. From (2.19) at $y \to \infty$ we have

$$\begin{Bmatrix} \tilde{u} \\ \tilde{v} \\ \tilde{w} \\ \tilde{\theta} \\ \tilde{p} \\ \tilde{u}' \\ \tilde{w}' \\ \tilde{\theta}' \end{Bmatrix} = \sum_{i=1}^{4} C_i \boldsymbol{q}_i \, \mathrm{e}^{-\mu_i y}. \tag{2.36}$$

We have eight equations with four unknowns C_1, C_2, C_3 and C_4. Eliminating C_1, C_2, C_3 and C_4 we obtain four necessary boundary conditions at the far field in terms of $\{\tilde{u}, \tilde{v}, \tilde{w}, \tilde{\theta}, \tilde{p}, \tilde{u}', \tilde{w}', \tilde{\theta}'\}$. Here prime denotes differentiation with respect to y.

We use Briggs (1964) method to invert (2.31) and evaluate $\boldsymbol{\phi}(x, y, z, t)$ for $t \to \infty$. For a detailed discussion of this method the reader is referred to the review by Bers (1983). The function $\tilde{\boldsymbol{\Phi}}$ is analytic above the contour L in the ω-plane and is analytic in the strips close to contours F and J. In the Briggs method the F, L contours are methodically shifted to contours $\tilde{F}, \tilde{L}$ (see figure 2). After this is done the same analytic behaviour is preserved. The function $\tilde{\boldsymbol{\Phi}}$ is analytic above $\tilde{L}$ and in the strips close to $\tilde{F}$ and J. To find the finite-time solution, we need to evaluate the integral in (2.31) numerically. This involves three integrals: one in the ω-plane, one in the k_x-plane and one in the k_z-plane. By seeking solution for $t \to \infty$ and shifting these contours F, L we simplify the integral in the ω-plane to the residue integrals and hence reduce the number of integrals from three to two. In other words, we essentially transform the temporal problem into a spatial one.

This deflection of contours is admissible only if there is no absolute instability. We assume that the boundary layers we consider do not have absolute instability. First we perform the inversion from k_x to x according to

$$I(x, y, k_z, \omega) = \frac{1}{2\pi} \int_{\tilde{F}} \mathrm{e}^{\mathrm{i}k_x x} \tilde{\boldsymbol{\Phi}}(k_x, y, k_z, \omega) \, \mathrm{d}k_x. \tag{2.37}$$

To evaluate the integral we construct closed contours in the k_x-plane and apply the residual theorem.

For $x > 0$

$$I(x, y, k_z, \omega) = \frac{1}{2\pi} \left\{ \sum \mathrm{e}^{\mathrm{i}k_x^{\mathrm{u}}(\omega) x} 2\pi\mathrm{i} \frac{1}{\left\{ \frac{\partial}{\partial k_x}\left(\frac{1}{\tilde{\boldsymbol{\Phi}}}\right) \right\}_{k_x^{\mathrm{u}}(\omega)}} + V_{\mathrm{B}}^{\mathrm{u}}(x, y, k_z, \omega) \right\}, \tag{2.38}$$

and for $x < 0$

$$I(x, y, k_z, \omega) = \frac{1}{2\pi} \left\{ \sum -\mathrm{e}^{\mathrm{i}k_x^1(\omega)x} 2\pi\mathrm{i} \frac{1}{\left\{ \frac{\partial}{\partial k_x}\left(\frac{1}{\tilde{\Phi}}\right)\right\}_{k_x^1(\omega)}} + V_{\mathrm{B}}^1(x, y, k_z, \omega) \right\}, \quad (2.39)$$

where $k_x^{\mathrm{u}}(\omega)$ is the location of poles of $(1/\tilde{\Phi})$ in the plane above $\tilde{F}$, while $k_x^1(\omega)$ represents the poles in the plane below $\tilde{F}$. Also, $V_{\mathrm{B}}^{\mathrm{u}}$ and $V_{\mathrm{B}}^1(\omega)$ represent the contributions from the integral around the branch cuts in the planes above and below the $\tilde{F}$ contour, respectively.

Next we perform the inversion from ω to t:

$$\tilde{I}(x, y, k_z, t) = \frac{1}{2\pi} \int_{\tilde{L}} -\frac{\omega_0}{\omega^2 - \omega_0^2} \mathrm{e}^{-\mathrm{i}\omega t} I(x, y, k_z, \omega) \, \mathrm{d}\omega. \quad (2.40)$$

Owing to the carefully selected contour $\tilde{L}$ in figure 2 (d), when $t \to \infty$ only the integrals around the singularities $\omega = \pm \omega_0$ contribute to $\tilde{I}(x, y, k_z, t)$. Thus, we obtain

$$\tilde{I}(x, y, k_z, t) = \frac{1}{2\pi}\{ -\pi\mathrm{i}\mathrm{e}^{\mathrm{i}\omega_0 t} I(x, y, k_z, -\omega_0) + \pi\mathrm{i}\mathrm{e}^{-\mathrm{i}\omega_0 t} I(x, y, k_z, \omega_0)\} \quad (2.41)$$

since $I(x, y, k_z, \omega_0) = \bar{I}(x, y, k_z, -\omega_0)$ where $\bar{I}$ is the conjugate of I we obtain

$$\tilde{I}(x, y, k_z, t) = \frac{1}{2\pi} \mathrm{Re}\, [2\pi\mathrm{i}\mathrm{e}^{-\mathrm{i}\omega_0 t} I(x, y, k_z, \omega_0)]. \quad (2.42)$$

Finally, the inversion from k_z to z is given as

$$\phi(x, y, z, t) = \frac{1}{2\pi} \int_J \mathrm{e}^{\mathrm{i}k_z z} \tilde{I}(x, y, k_z, t) \, \mathrm{d}k_z. \quad (2.43)$$

Substituting for $\tilde{\Phi}$ from (2.32) we can show that

$$\frac{\mathrm{i}}{\left\{ \frac{\partial}{\partial k_x}\left(\frac{1}{\tilde{\Phi}}\right)\right\}_{k_x^{\mathrm{u}}(\omega)}} = C(k_x, k_z, \omega)\, \tilde{\psi}(k_x, y, k_z, \omega)|_{k_x^{\mathrm{u}}(\omega)}. \quad (2.44)$$

Here $\tilde{\psi}(k_x, y, k_z, \omega)$ is the eigenfunction of the stability equations corresponding to the eigenvalue $k_x^{\mathrm{u}}(\omega)$, and $C(k_x, k_z, \omega)$ is the associated receptivity coefficient which is computed from the relation

$$C(k_x, \kappa_z, \omega) = \frac{\mathrm{i}}{\tilde{\psi}(k_x, y, k_z, \omega) \frac{\partial}{\partial k_x}\left(\frac{1}{\tilde{\Phi}}\right)\Big|_{k_x^{\mathrm{u}}(\omega)}}. \quad (2.45)$$

This coefficient gives the initial amplitude of the discrete modes which are generated by the point source. In order to study the downstream evolution of these modes in a growing boundary layer (in a following paper) we will use this as the initial condition.

3. Results

We have performed calculations for two-dimensional supersonic boundary layers at $Re = 1000$. The following two specific cases were considered: (i) $M = 2$, $\omega_0 = 0.02$; (ii) $M = 4.5$, $\omega_0 = 0.2$. Adiabatic wall conditions and a free-stream stagnation temperature of 311 K were assumed. Viscosity was computed using Sutherland's law. Boundary-layer thicknesses scaled with $(\nu_\infty x_0/U_\infty)^{\frac{1}{2}}$ were computed to be 7.6 and
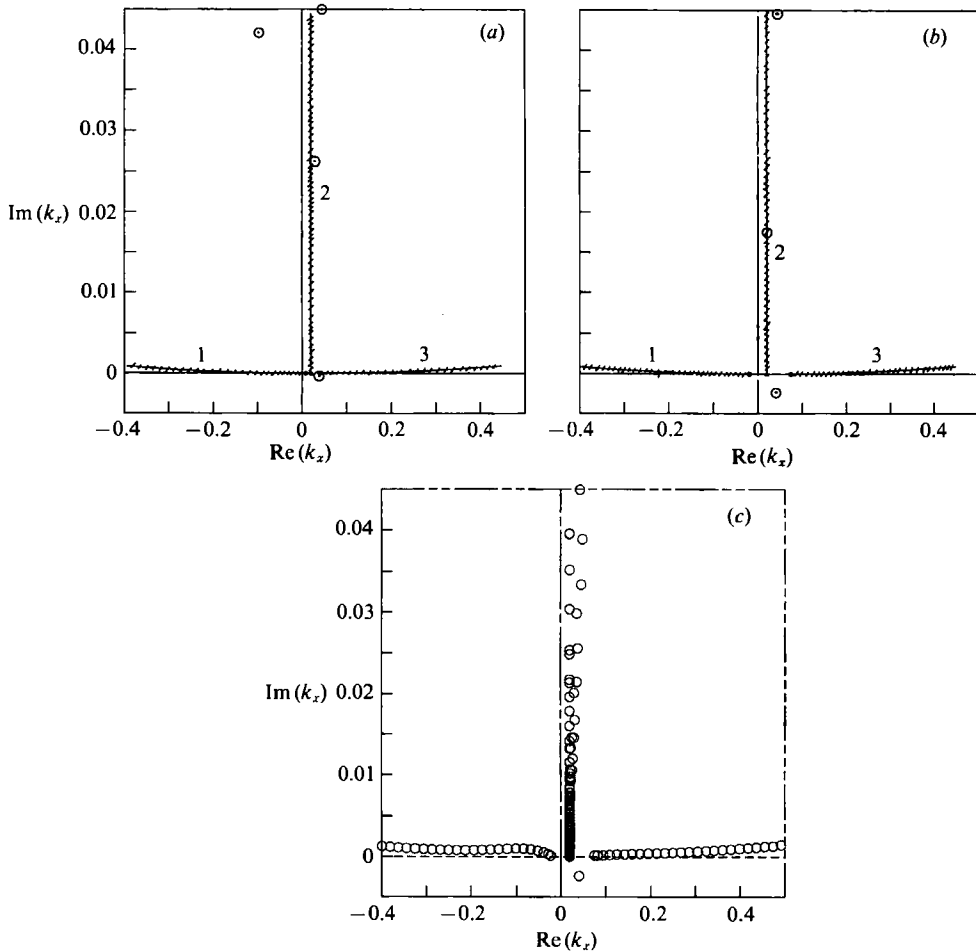
FIGURE 3. Branch cuts and poles in the complex k_x-plane at $Re = 1000$, $M = 2$, $\omega = 0.02$; and (a) $k_z = 0$, (b) $k_z = 0.08$. The points show some of the least-stable eigenvalues given by $\Delta = 0$. (c) Eigenvalue spectrum from the global method for the same parameters as (b).

14.6, respectively. The governing equations, (2.33), were solved using a fourth-order-accurate two-point compact scheme (Malik, Chuang & Hussaini 1982).

First we present the branch cuts and the poles which exist in the complex k_x-plane. For a fixed k_z and ω, the branch cuts in the $\lambda_i (i = 1, 4)$ planes (2.20)–(2.22) are mapped in the k_x-plane according to the formulae

$$-\lambda_{10} = \mathrm{i}(k_x - \omega)Re + k_x^2 + k_z^2, \tag{3.1}$$

$$-\lambda_{30} = \tfrac{1}{2}[b_{22} + b_{33} + [(b_{22} + b_{33})^2 + 4(b_{23}b_{32} - b_{22}b_{33})]^{\frac{1}{2}}], \tag{3.2}$$

$$-\lambda_{40} = \tfrac{1}{2}[b_{22} + b_{33} - [(b_{22} + b_{33})^2 + 4(b_{23}b_{32} - b_{22}b_{33})]^{\frac{1}{2}}], \tag{3.3}$$

where $0 \leqslant \lambda_{10}, \lambda_{30}, \lambda_{40} \leqslant \infty$.

Equation (3.1) can be solved for k_x to yield

$$k_x = -\tfrac{1}{2}\mathrm{i}Re \pm \tfrac{1}{2}\mathrm{i}[Re^2 + 4(\lambda_{10} + k_z^2 - \mathrm{i}\omega Re)]^{\frac{1}{2}}. \tag{3.4}$$

Combining (3.2) and (3.3) we can get a fifth-order polynomial equation for k_x which is solved numerically using an IMSL subroutine. Therefore, we have seven branch cuts in the complex k_x-plane, both for $k_z = 0$ and $k_z \neq 0$.

The results for the case $M = 2.0$, $\omega_0 = 0.02$, $Re = 1000$ are given in figure 3. Figure
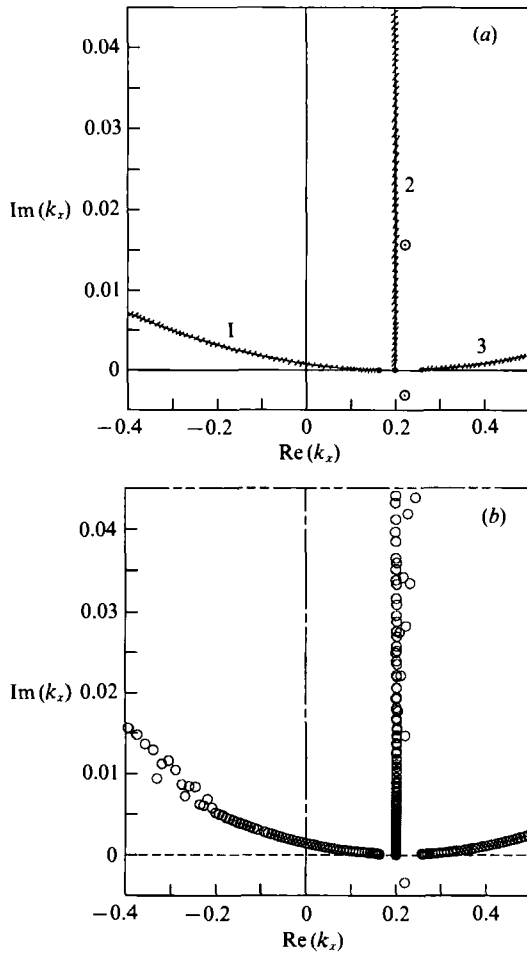
FIGURE 4. (a) Branch cuts and poles in the complex k_x-plane for $M = 4.5$, $\omega = 0.2$, $k_z = 0$, $Re = 1000$. (b) Eigenvalue spectrum from the global method for the same parameters as (a).

$3(a)$ shows the results for the spanwise wavenumber $k_z = 0$ and figure $3(b)$ is for $k_z = 0.08$. For comparison, we show the global eigenvalue spectrum for $k_z = 0.08$ in figure $3(c)$. We will discuss it later. Figure $4(a)$ shows the results for the case $M = 4.5$, $\omega_0 = 0.2$, $Re = 1000$ and $k_z = 0$ and figure $4(b)$ shows the corresponding results of the global eigenvalue calculations. For each case there exist seven branch cuts in the complex k_x-plane. We have shown only four of these in the plots. These are labelled 1, 2 and 3. Curves 1 and 3 represent acoustic waves, while curve 2 represents two branch cuts associated with vorticity and entropy waves. At the Reynolds number of 1000, the vorticity and entropy branch cuts have merged but they may be distinct at small Reynolds numbers. The other three branch cuts associated with the domain $x < 0$, have very large negative imaginary parts and, therefore, they do not appear in these graphs. The branch points of these seven branch cuts are given in table 1.

In the limit of large Reynolds number, the four roots (2.20)–(2.22) take the form

$$\lambda_1 = \lambda_2 = i(k_x - \omega)Re + k_x^2 + k_z^2, \tag{3.5}$$

$$\lambda_3 = i\sigma(k_x - \omega)Re, \tag{3.6}$$

$$\lambda_4 = k_x^2 + k_z^2 - (k_x - \omega)^2 M^2. \tag{3.7}$$

	(a)		(b)
$k_z = 0$	$k_z = 0.08$		$k_z = 0$
$(0.0133, 1.12 \times 10^{-7})$	$(-0.0214, 7.44 \times 10^{-6})$		$(0.1636, 2.069 \times 10^{-5})$
$(0.02, 4.00 \times 10^{-7})$	$(0.02, 6.80 \times 10^{-6})$		$(0.2, 4.0 \times 10^{-5})$
$(0.02, 5.55 \times 10^{-7})$	$(0.02, 9.44 \times 10^{-6})$		$(0.2, 5.55 \times 10^{-5})$
$(0.04, 3.02 \times 10^{-6})$	$(0.0747, 1.718 \times 10^{-5})$		$(0.2571, 8.03 \times 10^{-5})$
$(-0.02, -1000.0)$	$(-0.02, -1000.0)$		$(-0.2, -1000.0)$
$(-0.0204, -738.79)$	$(-0.0204, -738.79)$		$(-0.2014, -746.9)$
$(-0.0329, -391.56)$	$(-0.0329, -391.56)$		$(-0.219, -490.89)$

TABLE 1. Seven branch points in the k_x plane for the continuous spectrum in supersonic boundary layers at $Re = 1000$: (a) $M = 2.0$, $\omega_0 = 0.02$; (b) $M = 4.5$, $\omega_0 = 0.2$

We note that λ_4 is the root of the inviscid equation. By equating $\lambda_1 = \lambda_2 = \lambda_3 = \lambda_4 = 0$ we can obtain approximate expressions for five of the branch points in the limit of large Re. They are

$$\left(\frac{M^2\omega}{M^2-1} - \frac{1}{M^2-1} [(M^2-1)\,k_z^2 + \omega^2 M^2]^{\frac{1}{2}},\, 0 \right), \tag{3.8a}$$

$$(\omega, 0), \tag{3.8b}$$

$$(\omega, 0), \tag{3.8c}$$

$$\left(\frac{M^2\omega}{M^2-1} + \frac{1}{M^2-1} [(M^2-1)\,k_z^2 + \omega^2 M^2]^{\frac{1}{2}},\, 0 \right), \tag{3.8d}$$

$$(-\omega, -Re) \tag{3.8e}$$

These compare well with the values numerically computed for the first five branch points given in table 1. The acoustic branch cuts from the approximate roots will be along the real axis. Thus, the departure of curves 1 and 3 from the real axis in figure 3(a) indicates the level of correction at the Reynolds number of 1000. The approximate vorticity and entropy branch cuts will be vertical straight lines while curve 2 is expected to deviate from the vertical straight line at large values of $\mathrm{Im}\,(k_x)$. The branch points corresponding to

$$k_x = \frac{M^2\omega}{M^2-1} \mp \frac{1}{M^2-1} [(M^2-1)\,k_z^2 + \omega^2 M^2]^{\frac{1}{2}} \tag{3.9a}$$

have the phase speed in the wave direction given by

$$\frac{\omega}{(k_x^2 + k_z^2)^{\frac{1}{2}}} = \cos\theta \pm \frac{1}{M}, \tag{3.9b}$$

where θ is the wave angle given by $\tan\theta = k_z/k_x$. When $\theta = 0$ the phase speed becomes $\omega/k_x = 1 \pm 1/M$. We see that the wave is travelling at the speed of sound relative to the free-stream velocity in the θ-direction. The continuous spectrum branches associated with branch points (3.9a) are the acoustic waves. The continuous spectrum branches associated with the first two roots, λ_1, λ_2 (equation (3.5)), are the vorticity waves, λ_3 (equation (3.6)) gives the entropy wave, and λ_4 (equation (3.7)) gives the acoustic wave. The branch point corresponding to $k_x = \omega$ has phase speed equal to the free-stream velocity. We also observe in figures 3(a, b) and 4(a) that at the chosen Reynolds number one of the vorticity modes and one of the entropy modes come together in the upper half-plane. For computational purposes we consider these two branch cuts, labelled as curve 2, as a single branch cut in the

complex wavenumber space. Since the continuous spectrum in the lower half-plane has very large imaginary parts, its contribution will decay very rapidly in the upstream direction. Therefore, the upstream influence from localized disturbances in a supersonic boundary layer will be small compared to that in an incompressible flow.

In incompressible flows, there exist four branch cuts in the complex k_x-plane. The corresponding two roots in the incompressible case are given by (3.5) and (3.7) with $M = 0$. The roots from (3.7) are the solution to the Rayleigh equation while the roots from (3.5) include the effect of viscosity. The branch cuts from (3.7) appear along the imaginary axis with branch points at the origin. One of the branch cuts from (3.5) appears in the upper half-plane with the branch point at $(\omega, 0)$ and the other in the lower half-plane with branch points at $(-\omega, -Re)$. Therefore, both branch cuts (inviscid and viscous) in the upper half of the k_x-plane influence the flow field downstream of the source. Since the imaginary part of the viscous branch cut in the lower half-plane is large, only the inviscid branch cut influences the flow field in the upstream direction. Hence the ellipticity which is caused by the pressure introduces the upstream influence in incompressible flows. In compressible flows the inviscid branch cuts are shifted to the upper half-plane as shown in figure 3(a) (curves 1 and 3) which reflects the hyperbolic behaviour of the supersonic flows. Hence, the upstream influence is only due to the viscosity and consequently small. Since in incompressible flows the inviscid branch cuts are along the imaginary axis, the contribution from this solution appears as a standing wave pattern in the streamwise and normal directions.

In figures 3(a, b) and 4(a) we have also marked a few of the least stable eigenvalues given by the dispersion relation $\Delta = 0$. These are obtained by solving the linear stability equations using the Chebyshev spectral collocation method (Malik 1990). Some of the least stable eigenvalues are given in table 2. Also included are the values of the receptivity coefficient C. These receptivity coefficients are based upon the maximum amplitude of streamwise velocity fluctuations. We note that for the cases considered in this paper, the receptivity coefficients for the least stable mode are lower than those for the higher discrete modes.

Figures 3(c) and 4(b) contain the results computed by discretizing the stability equations (2.9) using Chebyshev spectral collocation technique and by employing the QR algorithm which solves the generalized eigenvalue problem for the discretized system. For clarity, we have only shown the results for the k_x domain used in figures 3(b) and 4(a), respectively. These eigenvalue calculations yield all the discrete modes and also attempt to reproduce the discretized version of the continuous spectrum. Comparison of figures 3(c) and 4(b) with 3(b) and 4(a) indicates that the global method does a fair job in reproducing the continuous spectra. In figure 3(c), the vorticity and entropy branches tend to diverge from each other, apparently owing to the lack of resolution. A total of 81 collocation points were used in a spectral multi-domain calculation. However, no attempt was made to optimize the grid distribution. For Mach 4.5 (figure 4b), 161 collocation points were used. Now the vorticity and entropy branches are closer to each other but the left acoustic branch shows some scatter at negative Re (k_x). For the results presented in figures 3(c) and 4(b), the free-stream computational boundary was assumed to be at $y = 100$ where zero perturbation conditions were imposed.

It may be pointed out that a global eigenvalue calculation may also yield spurious modes which will move when the number of collocation points is increased or when the location of the free-stream boundary is changed. In general, it is difficult to determine which of the eigenvalues obtained from the global calculation are true
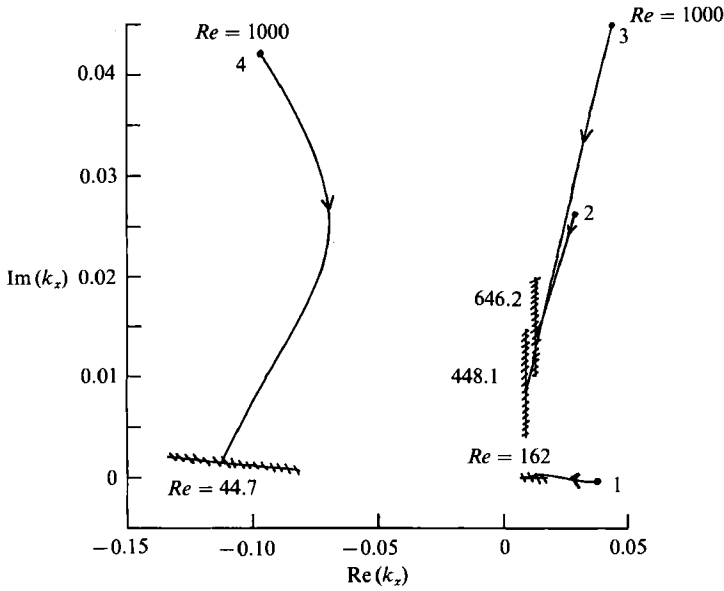
FIGURE 5. The variation of the eigenvalues as the Reynolds number is reduced from 1000 for $M = 2$, $\omega = 0.02$, $k_z = 0$, $F = 0.2 \times 10^{-4}$. The Reynolds numbers at which the discrete modes join various branches of the continuous spectrum are also shown.

(a)	$k_z = 0$		$k_z = 0.08$	
	k_x	$|C(k_x, k_z, \omega)|$	k_x	$|C(k_x, k_z, \omega)|$
	$(3.733 \times 10^{-2}, -3.696 \times 10^{-4})$	2.2079×10^{-2}	$(4.077 \times 10^{-2}, -2.384 \times 10^{-3})$	0.2333
	$(2.841 \times 10^{-2}, 2.619 \times 10^{-2})$	1.1448	$(2.035 \times 10^{-2}, 1.751 \times 10^{-2})$	11.9667
	$(-9.670 \times 10^{-2}, 4.206 \times 10^{-2})$	0.7527	$(4.382 \times 10^{-2}, 4.453 \times 10^{-2})$	0.2193
	$(4.366 \times 10^{-2}, 4.495 \times 10^{-2})$	4.7175×10^{-2}	$(-6.637 \times 10^{-2}, 7.634 \times 10^{-2})$	0.7404
(b)	$k_z = 0$		$k_z = 0.12$	
	k_x	$|C(k_x, k_z, \omega)|$	k_x	$|C(k_x, k_z, \omega)|$
	$(0.220, -3.091 \times 10^{-3})$	1.7537×10^{-2}	$(0.2181, 2.969 \times 10^{-4})$	1.5405×10^{-2}
	$(0.221, 1.569 \times 10^{-2})$	9.9071×10^{-2}	$(0.2124, 1.288 \times 10^{-2})$	6.1334×10^{-2}
	$(-0.565, 5.559 \times 10^{-2})$	0.3878	$(-0.5498, 5.684 \times 10^{-2})$	0.3862
	$(0.560, 5.659 \times 10^{-1})$	6.5089		

TABLE 2. Discrete modes and the corresponding receptivity coefficients at $Re = 1000$:
(a) $M = 2.0$, $\omega_0 = 0.02$; (b) $M = 4.5$, $\omega_0 = 0.2$

discrete modes and which are due to the continuum unless one knows where the continuous spectrum lies. However, the comparison of figure 4 (a, b) shows that a well-resolved global calculation can, at least, pick up parts of the continuous spectrum.

In figure 5 we plot the locus of the discrete modes in the k_x-plane when the Reynolds number is reduced from 1000. For an incompressible flow, calculations by Murdock & Stewartson (1977) showed that the discrete modes are absorbed into the continuous spectrum when Reynolds number is decreased. In figure 5 we observe the same behaviour in the compressible flow. This calculation was done for the case $M = 2$, $F = 0.2 \times 10^{-3}$ where F is the non-dimensional frequency, $F = \omega/Re$.
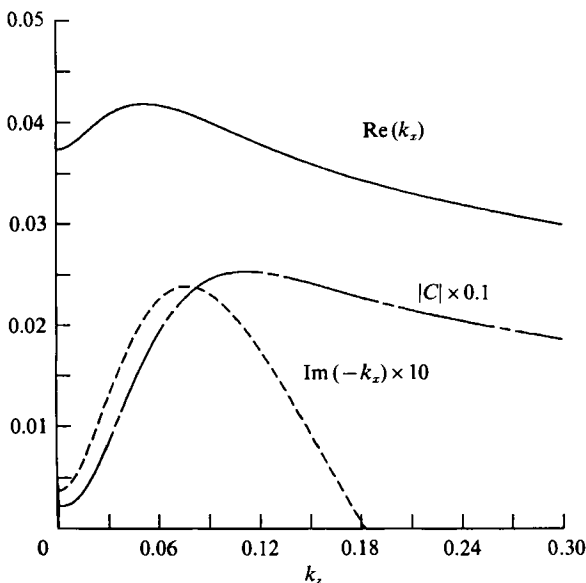
FIGURE 6. Eigenvalues k_x and receptivity coefficient $|C|$ (based on streamwise velocity) for $M = 2$, $\omega = 0.02$, $Re = 1000$.

Eigenvalues 1, 2, 3 and 4 are the four least stable modes at $Re = 1000$ as also shown in figure 3(a). We traced these modes by reducing the Reynolds number. These modes are absorbed into the continuous spectrum at the critical Reynolds numbers of 162, 646.2, 448.1 and 44.7 for modes 1, 2, 3 and 4, respectively. Also plotted is the continuous spectrum at those corresponding Reynolds numbers to show the merging of each discrete mode and the continuous spectrum. We also note that modes 1 and 4 merge with the acoustic wave continuous spectra and the modes 2, 3 merge with the vortical or the entropy wave continuous spectra. Thus, the least stable mode goes to the acoustic branch for the present case of $k_z = 0$.

There exists only one unstable eigenvalue for a given k_z. The variation of the least stable eigenvalue with spanwise wavenumber k_z is plotted in figures 6 and 7. Figure 6 shows the results for $M = 2.0$, $\omega_0 = 0.02$, $Re = 1000$ and figure 7 shows the results for $M = 4.5$, $\omega_0 = 0.2$, $Re = 1000$. The plots show the real and imaginary parts of the eigenvalue k_x and the amplitude of the receptivity coefficient C (see (2.45)). At $M = 4.5$, the receptivity coefficient is almost constant for most of the unstable k_z domain. The results in figures 6 and 7 show that a wide band of the k_z spectrum needs to be considered if the flow field near a localized source is to be accurately modelled.

Now, we present the computed results of $I(x, y, k_z, \omega_0)$, obtained from numerically integrating (2.37) along the contour $\tilde{F}$. We calculate $\tilde{\Phi} = (k_x, y, k_z, \omega_0)$ at selected grid points along $\tilde{F}$ and integrate (2.37) numerically. The contour $\tilde{F}$ is taken below the real axis and below the most unstable eigenvalue $k_x^u(\omega_0)$. Since $\tilde{\Phi} = (k_x, y, k_z, \omega_0)$ is singular at the points $k_x = k_x^u(\omega_0)$, a fine grid distribution is required in the region directly below $k_x = k_x^u(\omega_0)$ or the $\tilde{F}$-contour needs to be shifted well below $k_x^u(\omega_0)$. A simple way to remove this difficulty is to rewrite the integral in (2.37) in the following form, for $x > 0$,

$$I = \frac{1}{2\pi} \int_{\tilde{F}} e^{ik_x x} \left\{ \tilde{\Phi} - \frac{C(k_x, k_z, \omega_0)\, \psi(k_x, k_z, \omega_0, y)}{i(k_x - k_x^u(\omega_0))} \right\} dk_x$$
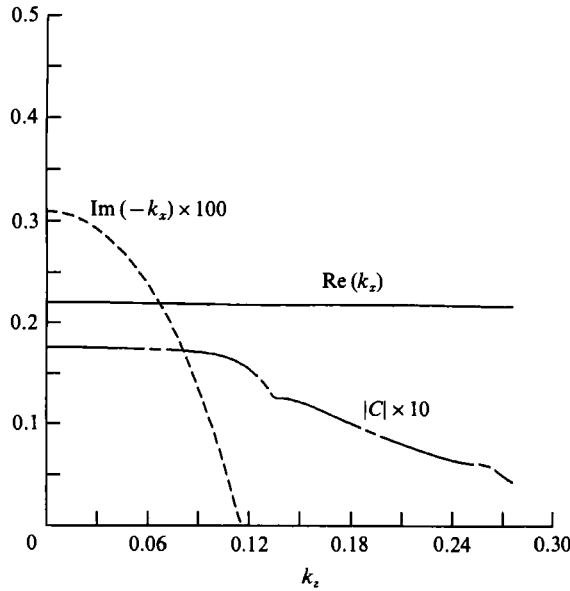$$+ \{e^{ik_x x} C(k_x, k_z, \omega_0)\, \psi(k_x, k_z, \omega_0, y)\}_{k_x^u(\omega_0)}, \quad (3.10)$$

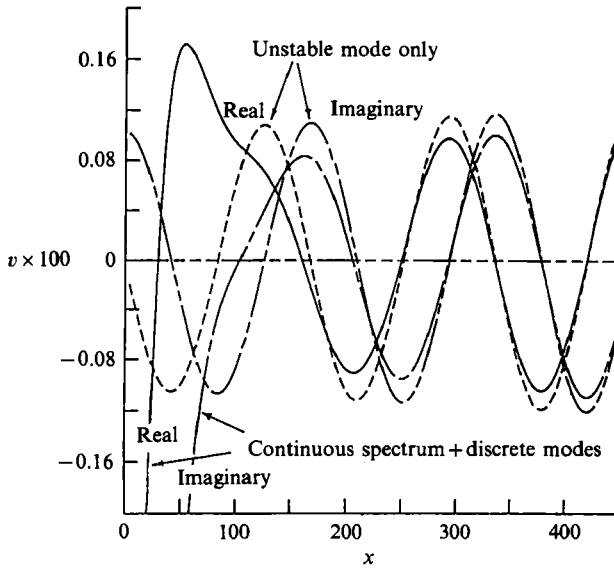FIGURE 7. Eigenvalues k_x and receptivity coefficient $|C|$ for $M = 4.5$, $\omega = 0.2$, $Re = 1000$.
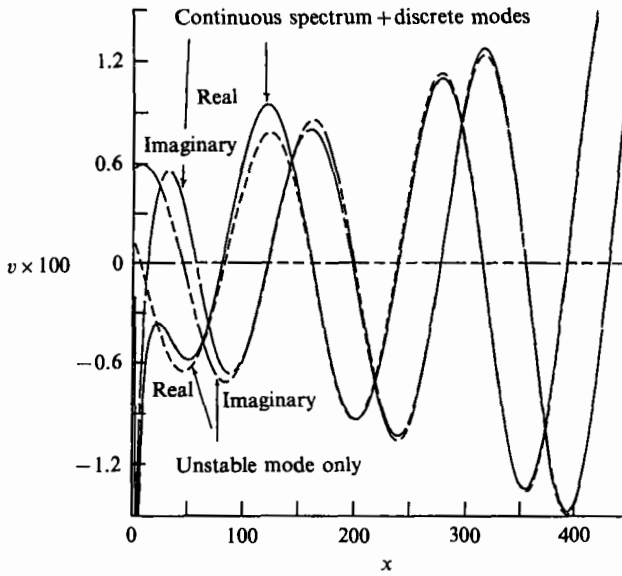
FIGURE 8. Normal velocity distribution at $y/(\nu_\infty x_0 U_\infty)^{\frac{1}{2}} = 2.3$ for $k_z = 0$,
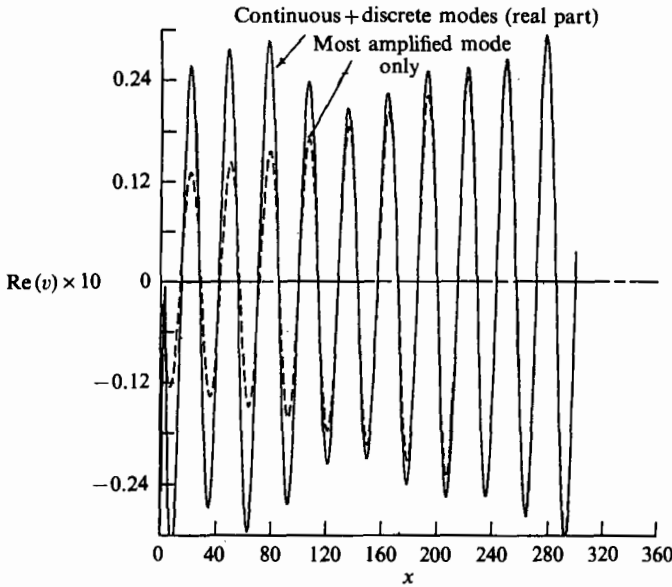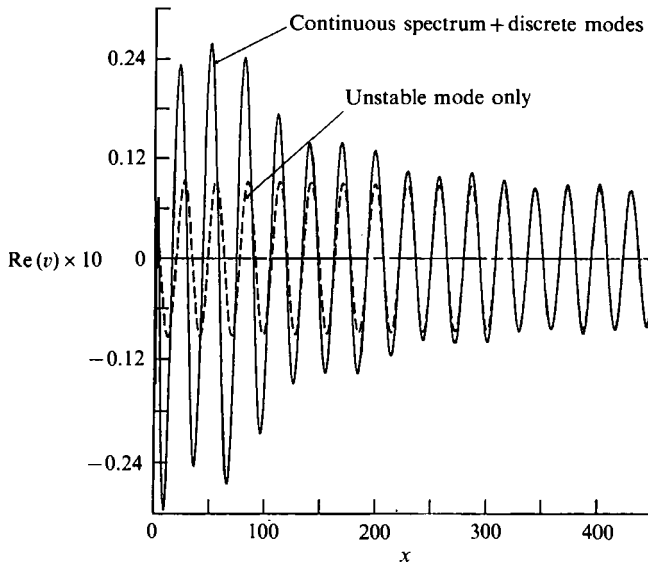$M = 2$, $\omega_0 = 0.02$, $Re = 1000$.

where k_x^u represents the most unstable mode. Now $\tilde{F}$ can be taken anywhere below the real axis. Since the integrand in (3.10) is a smoothly varying function, it can be evaluated without much difficulty. We compare solution I from (3.10) with the discrete mode contribution $\tilde{I}$, where

$$\tilde{I} = \{e^{ik_x x} C(k_x, k_z, \omega_0) \, \psi(k_x, k_z, \omega_0, y)\}_{k_x^u(\omega_0)}. \tag{3.11}$$

Here $\tilde{I}$ is computed for only the most amplified wave for a given k_z. The difference between I and $\tilde{I}$ comes from the contributions made by the continuous spectrum and the other stable eigenmodes.

FIGURE 9. Normal velocity distribution at $y \, (\nu_\infty x_0 U_\infty)^{\frac{1}{2}} = 2.3$ for $k_z = 0.08$, $M = 2$, $\omega = 0.02$, $Re = 1000$.

FIGURE 10. Normal velocity distribution at $y/(\nu_\infty x_0 U_\infty)^{\frac{1}{2}} = 5.2$ for $k_z = 0$, $M = 4.5$, $\omega = 0.2$, $Re = 1000$.

Here we present the result for the normal velocity component $v(x, k_z, \omega_0, y)$. Figures 8 and 9 show the result for I and $\tilde{I}$ at the height $y/(\nu_\infty x_0/U_\infty)^{\frac{1}{2}} = 2.3$ for the case $M = 2$, $\omega_0 = 0.02$ and $Re = 1000$. The abscissa x represents the distance from the source scaled with $(\nu_\infty x_0/U_\infty)^{\frac{1}{2}}$. Figure 8 shows the result for the spanwise wavenumber $k_z = 0$ and figure 9 shows the result for $k_z = 0.08$. In these figures, real and imaginary parts of I and $\tilde{I}$ are shown. As expected, the difference $(I - \tilde{I})$ is large near the source and decreases with increasing x. It also decreases slower for $k_z = 0$ than for $k_z = 0.08$.

FIGURE 11. Normal velocity distribution at $y/(\nu_\infty x_0 U_\infty)^{\frac{1}{2}} = 5.2$ for $k_z = 0.12$, $M = 4.5$, $\omega = 0.2$, $Re = 1000$.
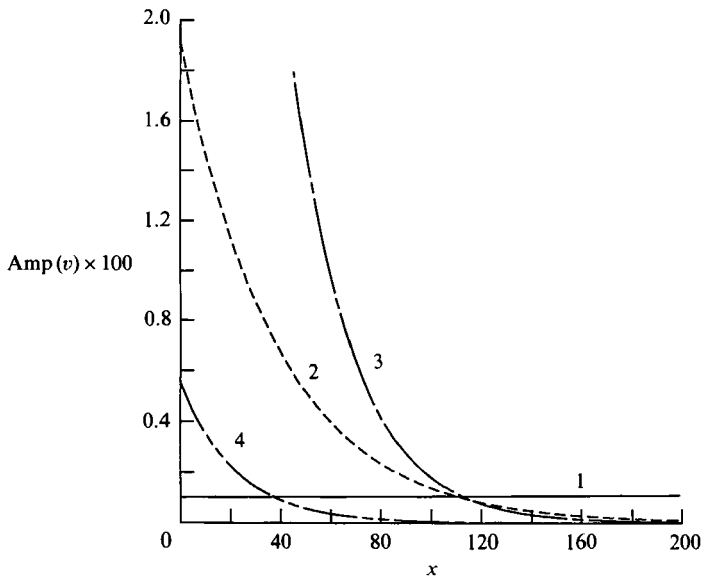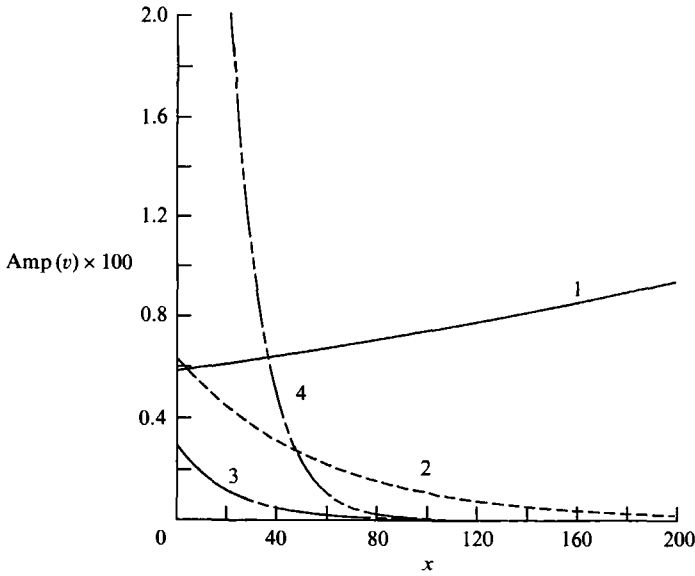

FIGURE 12. Contribution to normal velocity v at $y/(\nu_\infty x_0 U_\infty)^{\frac{1}{2}} = 2.3$ from discrete modes. $M = 2$, $k_z = 0$, $\omega_0 = 0.02$, $Re = 1000$. Curve 1 $(3.733 \times 10^{-2}, -3.696 \times 10^{-4})$; 2 $(2.841 \times 10^{-2}, 2.619 \times 10^{-2})$; 3 $(-9.670 \times 10^{-2}, 4.206 \times 10^{-2})$; 4 $(4.366 \times 10^{-2}, 4.495 \times 10^{-2})$.

Figures 10 and 11 show the result for I and $\tilde{I}$ at the height $y/(\nu_\infty x/U_\infty)^{\frac{1}{2}} = 5.2$ for the case $M = 4.5$ and $\omega_0 = 0.2$. Figure 10 shows the result for the spanwise wavenumber $k_z = 0$ and figure 11 shows the result for $k_z = 0.12$. Here also, the difference is larger near the source and it decreases with increasing x. In contrast with the first case, the difference $(I - \tilde{I})$ decreases more slowly for $k_z = 0.12$ than for $k_z = 0$. This is because at $M = 2$ the oblique mode is more unstable, while at $M = 4.5$ the two-dimensional second mode is more unstable.

FIGURE 13. Contribution to normal velocity v at $y/(\nu_\infty x_0 U_\infty)^{\frac{1}{2}} = 2.3$ from discrete modes. $M = 2$, $k_z = 0.08, \omega_0 = 0.02, Re = 1000$. Curve 1 $(4.077 \times 10^{-2}, -2.384 \times 10^{-3})$; 2 $(2.035 \times 10^{-2}, 1.751 \times 10^{-2})$; 3 $(4.382 \times 10^{-2}, 4.453 \times 10^{-2})$; 4 $(-6.638 \times 10^{-2}, 7.634 \times 10^{-2})$.

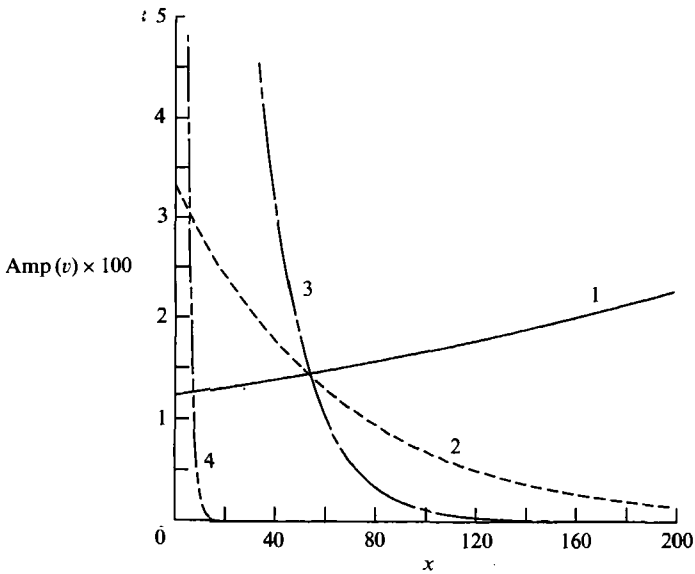FIGURE 14. Contribution to normal velocity v at $y/(\nu_\infty x_0 U_\infty)^{\frac{1}{2}} = 5.2$ from discrete modes. $M = 4.5$, $k_z = 0$, $\omega_0 = 0.2$, $Re = 1000$. Curve 1 $(0.220, -3.091 \times 10^{-3})$; 2 $(0.221, 1.569 \times 10^{-2})$; 3 $(-0.565, 5.559 \times 10^{-2})$; 4 $(0.560, 0.569 \times 10^{-1})$.

Next we present the contributions from various discrete eigenvalues computed using (3.11). In figures 12 and 13 we plot the amplitude of the v-velocity at the height $y/(\nu_\infty x_0/U_\infty)^{\frac{1}{2}} = 2.3$ for some of the discrete eigenvalues at $M = 2$. Figure 12 shows the result for $k_z = 0$ and figure 13 shows the result for $k_z = 0.08$. Figures 14 and 15 show the amplitude of the v-velocity at the height $y/(\nu_\infty x_0/U_\infty)^{\frac{1}{2}} = 5.2$ for $M = 4.5$, for $k_z = 0$ and $k_z = 0.12$ respectively. We observe that the amplitude of the v-velocity is, in general, much larger for the stable modes than for the unstable mode. For
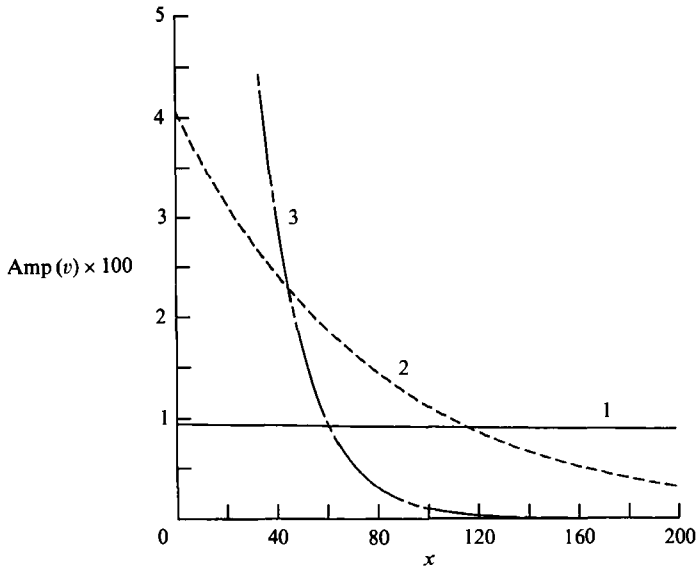
FIGURE 15. Contribution to normal velocity v at $y/(\nu_\infty x_0 U_\infty)^{\frac{1}{2}} = 5.2$ from discrete modes. $M = 4.5$, $k_z = 0.12$, $\omega_0 = 0.2$, $Re = 1000$. Curve 1 $(0.218, 2.969 \times 10^{-4})$; 2 $(0.212, 1.288 \times 10^{-2})$; 3 $(-0.549, 5.684 \times 10^{-2})$.

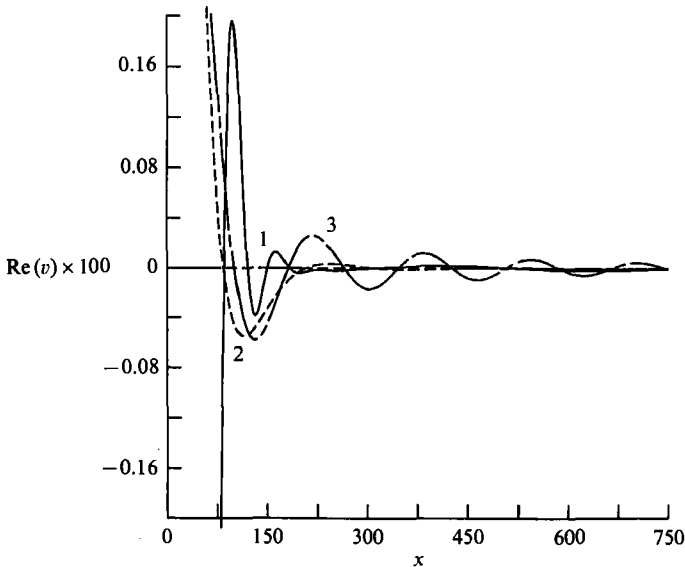FIGURE 16. Contribution to normal velocity at $y/(\nu_\infty x_0 U_\infty)^{\frac{1}{2}} = 2.3$ from continuous spectra 1, 2 and 3 of figure 3(a). $M = 2$, $k_z = 0$, $\omega_0 = 0.02$, $Re = 1000$.

$M = 2$ the amplitudes of stable modes are larger up to 15 boundary-layer thicknesses (for Mach 2, boundary-layer thickness scaled with $(\nu_\infty x_0/U_\infty)^{\frac{1}{2}}$ is 7.6; for Mach 4.5, it is 14.6) downstream for a two-dimensional wave, but for the three-dimensional wave the amplitude of the v-velocity remains larger than the unstable mode only up to 5 boundary-layer thicknesses. For $M = 4.5$ similar conclusions can be drawn. It is seen that the largest amplitude occurs for the eigenvalue with negative real part. This means that the wave with the phase speed in the negative x-direction has the largest
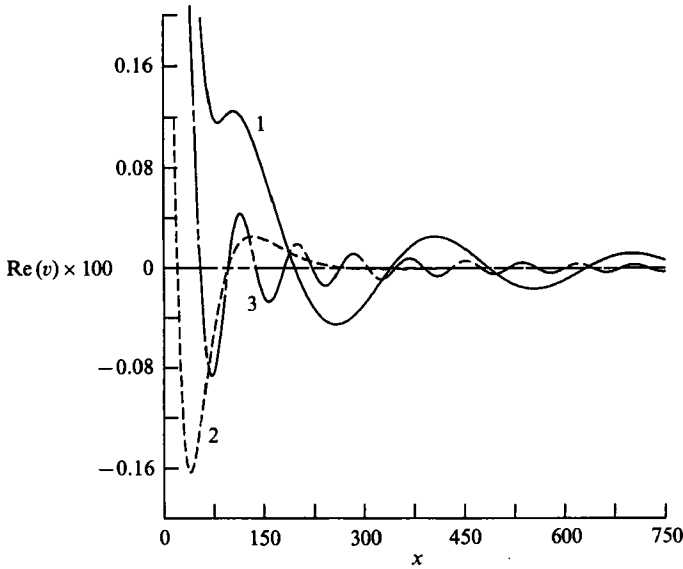
FIGURE 17. Contribution to normal velocity at $y/(\nu_\infty x_0 U_\infty)^{\frac{1}{2}} = 2.3$ from continuous spectra 1, 2 and 3 of figure 3(b). $M = 2$, $k_z = 0.08$, $\omega_0 = 0.02$, $Re = 1000$.

amplitude in the region near the source. While higher discrete modes may have larger amplitudes at the source (for example, Mode 4 for $k_z = 0$ in table 2(b) and figure 14) they have very high decay rates and, therefore, die off rapidly away from the source.

We point out that we have presented results for the velocity normal to the plate while experimentalists generally measure the fluctuating component parallel to the plate. However, the conclusions drawn here regarding the relative importance of various discrete modes and the continuous spectrum should carry over to the experimental situation.

The behaviour of the continuous spectrum near the source is now investigated. In figures 3 and 4, three branch cuts in the upper half of the complex k_x-plane were shown. Figures 16 and 17 show the contribution from these continuous spectra to the normal velocity v at the height $y/(\nu_\infty x_0/U_\infty)^{\frac{1}{2}} = 2.3$ for $M = 2.0$ at $k_z = 0$ and 0.08 respectively. The results are obtained by integrating the function

$$\frac{1}{2\pi} \int v \, \mathrm{e}^{\mathrm{i}k_x x} \, \mathrm{d}k_x \tag{3.12}$$

around the three branch cuts 1, 2 and 3. Similarly, figure 18 shows the results for $M = 4.5$ and $k_z = 0$. In all the cases, the contribution from the continuous spectrum is large near the source and decreases slowly downstream. The wavelengths of the oscillations downstream approximately equal the respective branch point values. For example, for $k_z = 0$ the wavenumbers of oscillation are approximately $M\omega/(M+1)$, ω and $M\omega/(M-1)$, which are the wavenumbers at the branch points 1, 2 and 3 respectively. As we discussed previously, the wave speeds corresponding to these branch points are $(U_\infty - a)$, U_∞, $(U_\infty + a)$ respectively where a is the speed of sound in the free stream. The waves with phase speeds $(U_\infty \pm a)$ are the acoustic waves and are the solution of the inviscid equations. However, the waves with phase speed U_∞ appear from the solution of the viscous equations. We also observe that the contribution from continuous spectrum branch 2 is small compared to the other two spectra. For $M = 2$ we see that the contribution from branch 3 has larger amplitudes
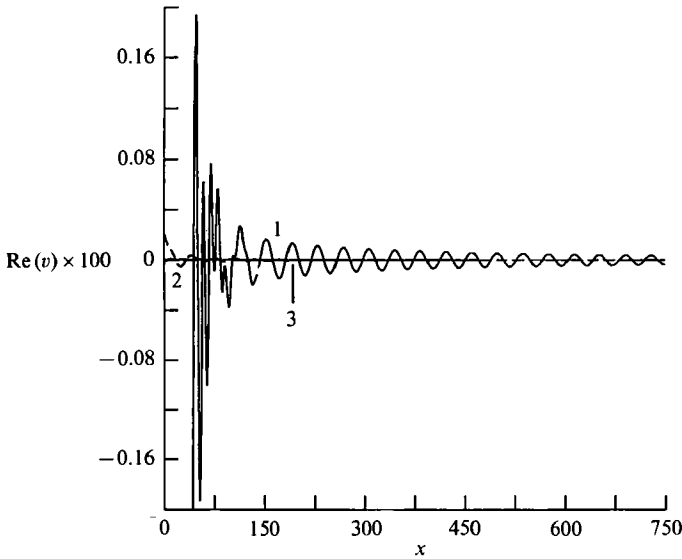
FIGURE 18. Contribution to normal velocity at $y/(\nu_\infty x_0 U_\infty)^{\frac{1}{2}} = 5.2$ from continuous spectra 1, 2 and 3 of figure 4. $M = 4.5$, $k_z = 0$, $\omega_0 = 0.2$, $Re = 1000$.
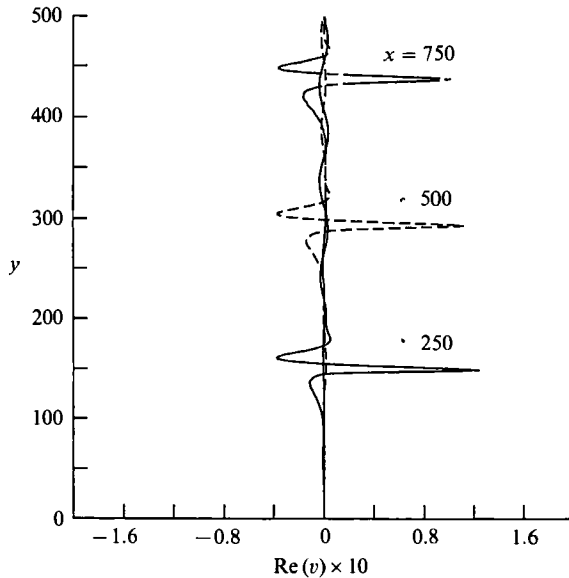

FIGURE 19. Variation of normal velocity v obtained from continuous spectrum 1 with y at x locations 250, 500, 750.

than the other two and at $k_z = 0.08$ branch 1 has larger amplitudes. At the higher Mach number $M = 4.5$ at $k_z = 0$ branch 1 contributes most to the disturbance field.

Figures 19–21 show the distribution of the v-velocity normal to the wall at the locations $x = 250, 500, 750$. Figure 19 shows the contribution from continuous branch 1 and figures 20 and 21 show the results for branches 2 and 3. As expected the continuous spectrum has larger disturbances outside the boundary layer than inside it. The peaks we observe in figures 19 and 21 are the Mach waves. Figure 20 $(a-c)$ shows the result for branch 2 which is associated with vorticity waves. It is interesting that they form a standing-wave-type pattern in the y-direction. However,
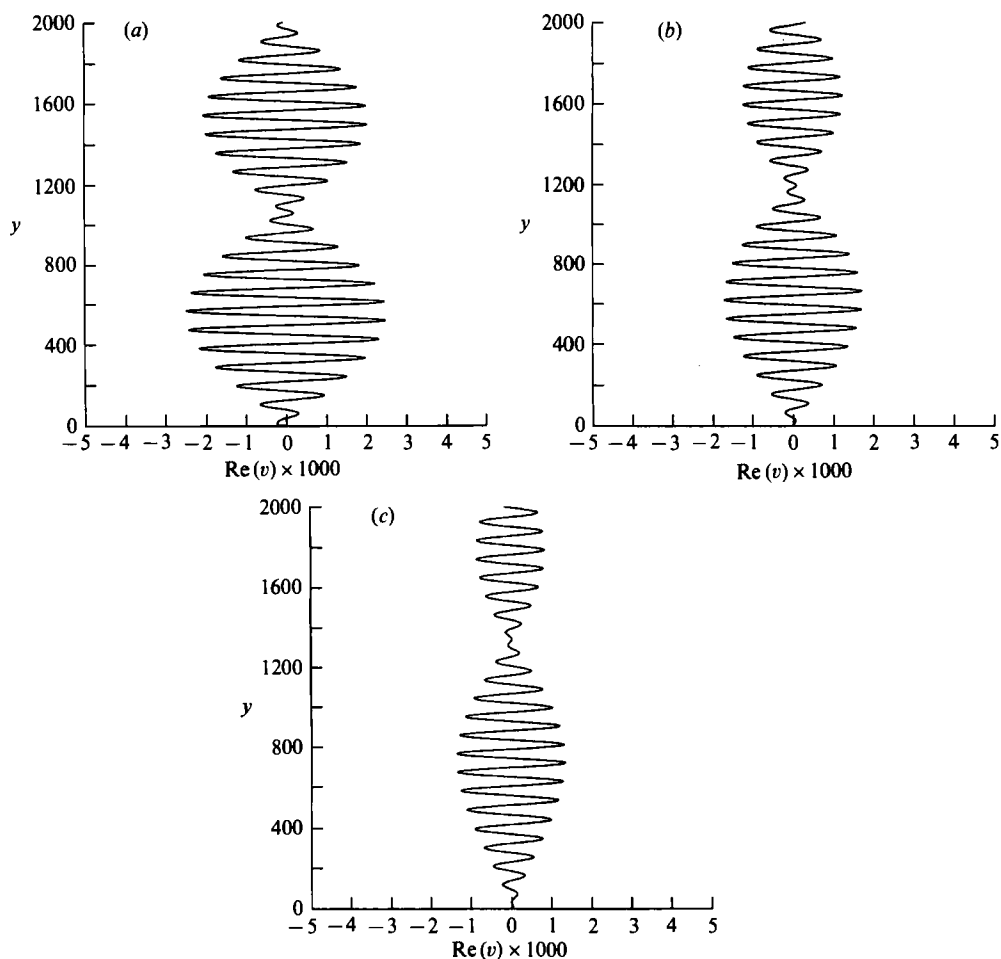
FIGURE 20. Variation of normal velocity v obtained from continuous spectrum 2 with y at x locations (a) 250, (b) 500, (c) 750.

the wave pattern moves in the free-stream direction with velocity U_∞. We also observe that the amplitude of the v-velocity in figure 20 is much lower than in figures 19 and 21.

Finally, we evaluate the solution $I(x, y, k_z, \omega)$ from equation (2.38). This expression consists of two terms: the first is the summation over all the discrete eigenmodes, and the second term is the contribution from the continuous spectrum. In figures 12–15 we showed the contribution from the discrete modes separately. In figures 16–18 we showed the contribution from the continuous spectrum. Hence, if we combine these two results we should obtain the magnitude of $I(x, y, k_z, \omega)$, which should be the same as shown in figures 8–11. Figures 22–24 show the results obtained using this procedure, i.e. adding the contribution from the discrete modes and continuous spectrum. We calculated the contribution from four of the least stable eigenmodes shown in table 2. Figures 22 and 23 show the result for $M = 2.0$, $k_z = 0$ and $k_z = 0.08$. Figure 24 shows the result for $M = 4.5$ and $k_z = 0$. As expected, we observe that figures 22–24 are essentially the same as figures 8–10, which confirms our numerical computation and shows that the solution near the source can be represented by the first few discrete modes and the continuous spectrum.
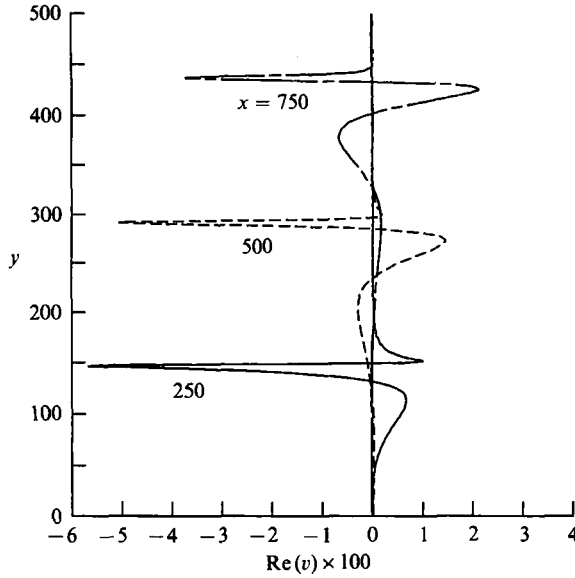
FIGURE 21. Variation of normal velocity v obtained from continuous spectrum 3 with y at x locations 250, 500, 750.
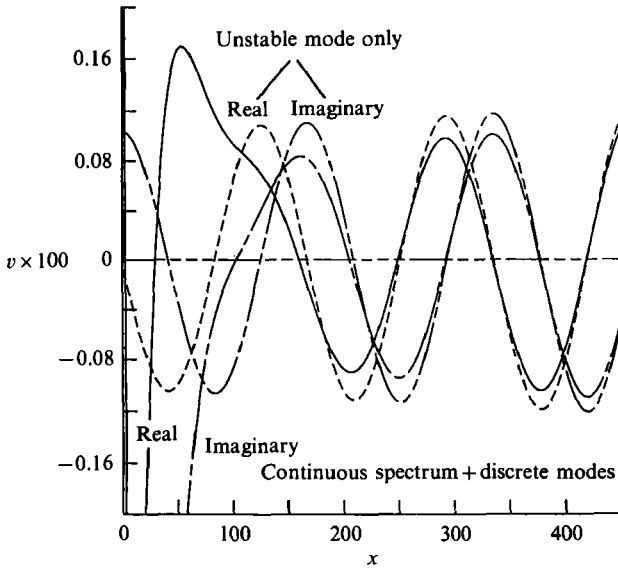

FIGURE 22. Normal velocity distribution obtained by summing discrete modes and continuous spectrum. $M = 2$, $\omega_0 = 0.02$, $k_z = 0$, $Re = 1000$.

4. Conclusions

We investigated the disturbance field near the source in supersonic boundary layers. The disturbances are introduced from a harmonic point source embedded in the wall. The solution consists of discrete modes and continuous spectra which are obtained using Fourier transform techniques. We find that there exist seven branch-cut singularities in the complex wavenumber space. Four of them are in the upper half-plane and the other three are in the lower half-plane. The spectrum in the lower half-plane have very large imaginary parts. Hence, the flow disturbance in the
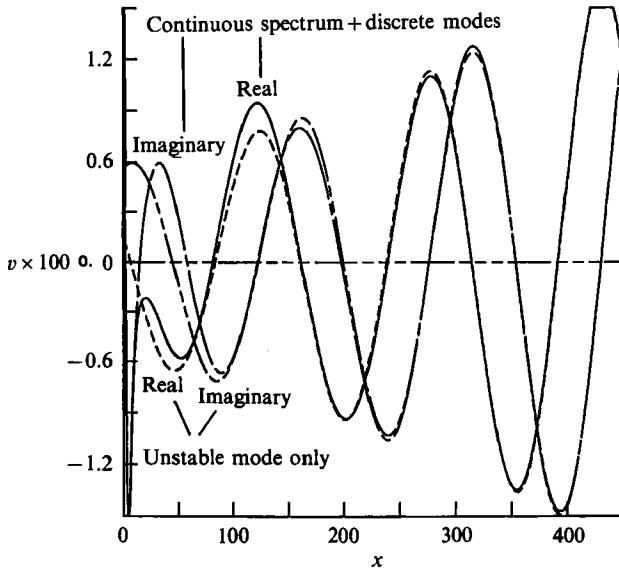
FIGURE 23. Normal velocity distribution obtained by summing discrete modes and continuous spectrum. $M = 2$, $\omega_0 = 0.02$, $k_z = 0.08$, $Re = 1000$.
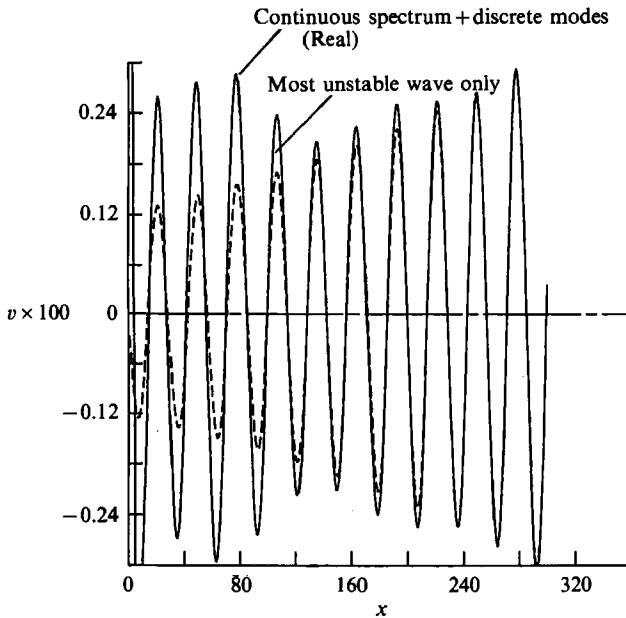

FIGURE 24. Normal velocity distribution obtained by summing discrete modes and continuous spectrum. $M = 4.5$, $\omega_0 = 0.2$, $k_z = 0$, $Re = 1000$.

upstream direction will decay over a small distance. Therefore, in a supersonic boundary layer the upstream influence from a localized disturbance is minimal.

The four branch cuts in the upper half of the plane contribute to the flow field downstream of the source. Two of these branch cuts are acoustic waves, one is a vorticity wave, and one is an entropy wave. At high Reynolds number the branch cuts for the vorticity wave and the entropy wave are close together and appear as one branch cut. The phase speed of the vorticity and entropy waves is equal to the free-

stream velocity. The phase speed at the branch points of the acoustic waves equals the speed of sound relative to the free-stream velocity.

In all the cases the contribution from these continuous spectra is large closer to the source and decays slowly in the downstream direction. The results also show that the disturbance from the continuous spectrum is larger outside the boundary layer than inside it. The contributions from the acoustic modes are confined to the region between the wall and the Mach wave originating from the source. The contribution from the vorticity and entropy waves produces a standing wave pattern in the direction normal to the wall.

We evaluated the contribution from the first few least-stable discrete modes. We observed that the contribution to the solution from the stable discrete modes is much larger near the source than that from the most unstable mode. Since these stable modes decay in the downstream direction, eventually the unstable mode will become dominant in the far field. Therefore, if the source is located near the neutral or stable region, up to several boundary-layer thicknesses, 15–20, the contribution from the stable discrete modes will be larger than that from the most unstable one. In other words, the near field of a vibrating point source may extend quite far downstream and measurements may be contaminated if they are made in this region.

It is also verified that the flow field near the source is represented by the continuous spectrum and the first few least-stable discrete modes. By tracing these discrete modes in the wavenumber space and by reducing the Reynolds number, it is established that these discrete modes spring off from the continuous spectrum.

Our results seem to suggest that, just like incompressible flow, there are only a finite number of discrete modes in supersonic flat-plate flow. A proof of the finiteness of the discrete spectrum is lacking for compressible flows. Finally, we have performed linear analysis using the parallel-flow approximation. It will be interesting to see how our conclusions will be altered when these assumptions are relaxed. However, such an analysis does not appear to be a straightforward extension of the present work.

REFERENCES

ASHPIS, D. E. & RESHOTKO, E. 1990 *J. Fluid Mech.* **213**, 531.

BERS, A. 1983 *Plasma Physics I* (ed. A. A. Galeev & R. N. Sudan), p. 451. North-Holland.

BRIGGS, R. J. 1964 *Electron-Stream Interaction with Plasmas*. MIT Press.

DiPRIMA, R. C. & HABETLER, G. J. 1969 *Arch. Rat. Mech. Anal.* **34**, 218.

GASTER, M. 1965 *J. Fluid Mech.* **22**, 433.

GROSCH, C. E. & SALWEN, H. 1978 *J. Fluid Mech.* **87**, 33.

GUSTAVSSON, L. H. 1979 *Phys. Fluids* **22**, 1602.

HENNINGSON, D. S. & SCHMID, P. J. 1991 *SIAM J.* (to appear).

MACK, L. M. 1976 *J. Fluid Mech.* **73**, 497.

MIKLAVCIC, M 1983 *Arch. Rat. Mech. Anal.* **83**, 221.

MIKLAVCIC, M. & WILLIAMS, M. 1982 *Arch. Rat. Mech. Anal.* **80**, 57.

MALIK, M. R. 1990 *J. Comput. Phys.* **86**, 376.

MALIK, M. R., CHUANG, S. & HUSSAINI, M. Y. 1982 *Z. Angew. Math. Phys.* **33**, 189.

MURDOCK, J. W. & STEWARTSON, K. 1977 *Phys. Fluids* **20**, 1404.

SALWEN, H. & GROSCH, C. E. 1981 *J. Fluid Mech.* **104**, 445.

TUMIN, A. M. & FEDOROV, A. V. 1983 *Prikl. Mat. Tech. Fiz.* **24**, 110 (transl. *J. Appl. Mech. Tech. Phys.* **548**, 1984).